iScience

CellPress
OPEN ACCESS

Article

Differential effects of sugar and fat on adipose tissue inflammation

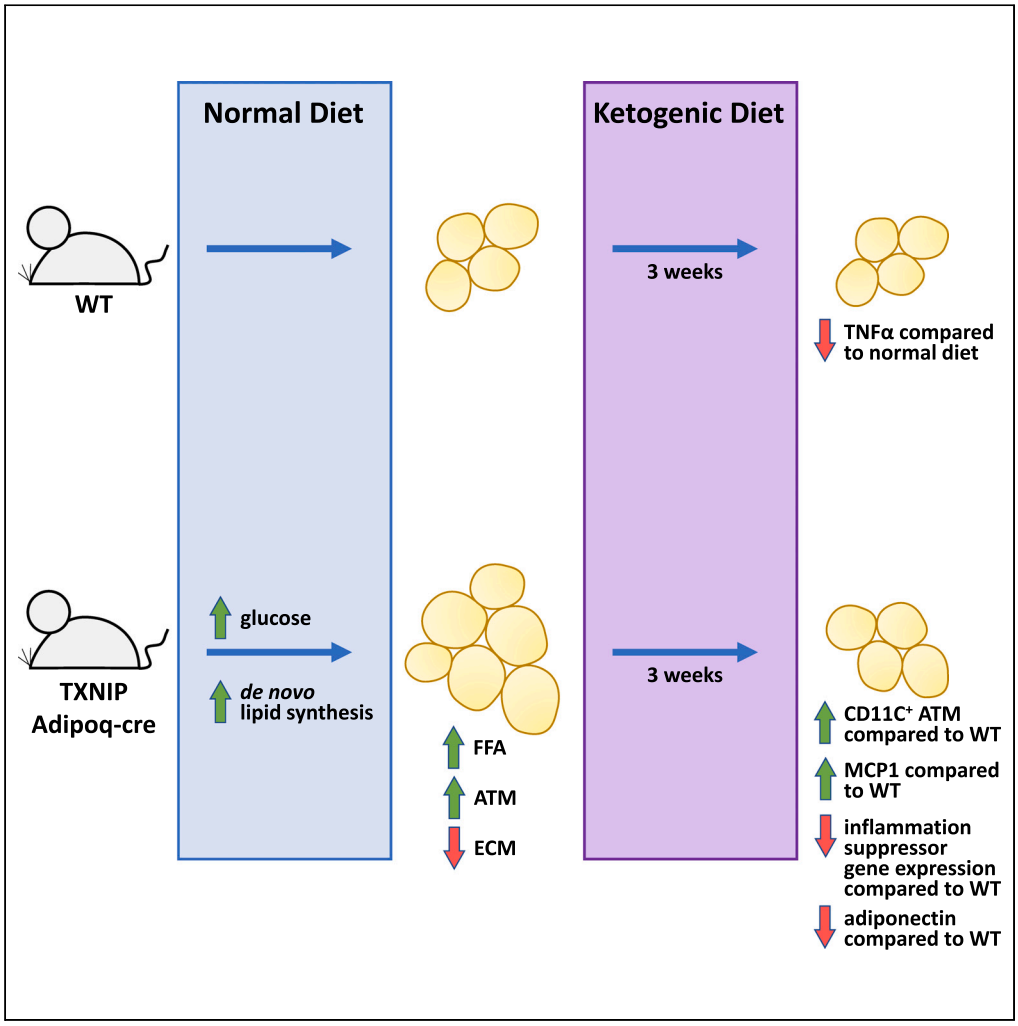

Tracey Avequin, Kin H. Lau, Althea N. Waldhart, Hannah Guak, Holly Dykstra, Connie Krawczyk, Ning Wu

ning@omnispacemail.com

Highlights

ATM number and ATM proinflammatory activation are regulated separately

Adipocytes respond differently to excess glucose or lipids

Excess glucose alone is insufficient to elicit full adipose tissue inflammation

Avequin et al., iScience *26*, 107163
July 21, 2023
https://doi.org/10.1016/j.isci.2023.107163

iScience

CellPress
OPEN ACCESS

Article

Differential effects of sugar and fat on adipose tissue inflammation

Tracey Avequin,[1] Kin H. Lau,[1] Althea N. Waldhart,[1] Hannah Guak,[2] Holly Dykstra,[1] Connie Krawczyk,[1] and Ning Wu[1,3,*]

SUMMARY

Obese individuals experience low grade inflammation initiated within their adipose tissue. However, the early events that lead to the release of these inflammatory factors from adipose tissue are poorly characterized. To separate glucose effects from lipid effects on adipose tissue, we used an adipose-specific TXNIP knockout model where excess basal glucose influx into adipocytes led to modest increase in adiposity without using high fat diet. We found an uncoupling of two events that are generally presumed to be coregulated: (1) an increase of adipose tissue macrophage (ATM) number; and (2) pro-inflammatory activation of ATMs. These two events are associated with different triggering signals: elevated free fatty acids output and extracellular matrix remodeling with increased ATM number, whereas decreased adiponectin level with activated ATM. This separation reflects non-overlapping pathways regulated by glucose and lipids in adipocytes, and neither group alone is sufficient to elicit the full inflammatory response in adipose tissue.

INTRODUCTION

Obesity has become a worldwide pandemic.[1] It is associated with chronic low-grade inflammation, which is a contributing factor for long-term development of diabetes and cardiovascular complications. Many of the pro-inflammatory factors that lead to those outcomes in obese individuals are secreted by white adipose tissue, a designated storage organ for lipids. Different cell types in adipose tissue are involved in generating and amplifying these factors, including the associated adipose tissue macrophages (ATM).[2–4] However, it is currently unclear at which point the storage cells, specifically the adipocytes themselves, reach their limit and send out these initial stress signals. Part of the problem is the common use of high fat diet (HFD) in diet-induced obesity studies. Although this diet can capture the human obese phenotypes in animals, it is difficult to decipher whether the diet is affecting each individual cell type directly or indirectly via expanded adipocytes. The effect of HFD on intestinal integrity and microbiota also complicates the situation by introducing possible bacterial antigens.[5,6] Furthermore, this diet does not allow clear separation of carbohydrate and lipid effects in mechanistic details. It is not even known if excess carbohydrates have the same or different effects on adipocytes as excess lipids, given that both provide extra calories and both are ultimately stored as lipids by adipocytes. Given the recent reports on the health benefits of short-term ketogenic diets,[7,8] there is a clear need to increase our understanding of the specific effects of excess carbohydrates on adipose tissue.

Carbohydrates constitute the major food group in the government dietary guidelines for Americans with glucose being arguably the most tightly regulated energy source in our blood. Excess carbohydrates are converted into lipids for storage in the adipose tissue, leading to adipose tissue expansion. To study the specific effect of glucose alone on adipose tissue health, we used the adipose-specific TXNIP knockout model *Txnip*$^{\Delta Adipoq}$ (AKO).[9–13] TXNIP is an α-arrestin protein that acts as an adaptor to GLUT4 to facilitate its endocytosis via the clathrin-coated pathway. When GLUT4 is needed on the cell surface, TXNIP is phosphorylated by AKT on insulin stimulation to dissociate it from GLUT4 and stop the endocytic process.[14] Specifically, knocking out TXNIP using adiponectin-cre should then result in increased glucose uptake in adipocytes only and not affect glucose uptake within other cell types associated with adipose tissue.[15,16] This allows us to create enlarged adipocytes in the AKO mice using only normal chow, thus avoiding the potential calorie overload of other cell types in the adipose tissue that can occur using HFD. In addition, we can use a ketogenic diet as a metabolic rescue to focus on changes specific to glucose, because this

[1]Van Andel Institute, Grand Rapids, MI 49503, USA

[2]Department of Pediatrics, University of Michigan, Ann Arbor, MI 48109, USA

[3]Lead contact

*Correspondence: ning@omnispacemail.com

https://doi.org/10.1016/j.isci.2023.107163

diet reduces the overall glucose usage, including by adipocytes, minimizing the differences between the wild type (WT) and AKO mice. Herein, we report the results of these studies, including the unexpected finding that ATM count and ATM pro-inflammatory activation are separately regulated events, with glucose and lipids modulating different aspects of full ATM activation.

RESULTS

AKO mice are modestly obese

At age 3 months, AKO male mice on C57B6/J background had higher fat mass than WT male mice (littermate matched control mice), whereas their body weight and lean mass were comparable (Figure 1A). This modest increase in adiposity still held at age 6 months. Increased fatty acids synthesis in AKO was confirmed through increased expression of FASN, ACC1/2, and ACLY as shown by western blot (Figure 1B). ACC1 is the cytoplasmic isoform of ACC that is involved in lipid synthesis whereas ACC2 is the isoform in mitochondria which regulates fatty acids oxidation. qPCR quantification confirmed increased expression of *Acaca* (ACC1) in AKO (Figure 1C). Consistent with increased lipid synthesis, average adipocyte sizes were larger in AKO relative to WT (Figures 1D and 1E). However, increased crown-like structures related to adipocyte apoptosis were not observed, suggesting that AKO adipose tissue was in an early stage of expansion.

Further metabolic phenotyping presented no difference in fasting blood glucose levels between WT and AKO animals at these ages (Figure 1F). Fasting plasma triacylglycerides (TAG) was higher in AKO beginning at 3 months (Figure 1G), whereas higher FFA levels reached significance at age 6 months (Figure 1H). We did not detect any difference in cholesterol levels at age 6 months between WT and AKO mice (Figure 1I). Previously, we had performed oral glucose tolerance tests (OGTT) on 3-month-old AKO. mice and showed that these mice exhibited a slightly faster decrease in glucose levels than the WT mice.[16] This difference in glucose response still held true for 6-month-old males (Figure 1J). For these mice, increased TAG was also found in the liver of AKO mice, but liver FFA stayed the same (Figures 1K and 1L). These data suggest that, in AKO mice, excess glucose leads to increased lipid synthesis in adipocytes compared to WT. Enlarged adipocytes output more FFAs into the circulation while simultaneously decreasing uptake of TAG from the liver to reduce its TAG storage. Together, these changes result in higher levels of plasma TAG and more TAG stored in the liver.

Along with increased adiposity, we wanted to examine whether the major adipokines had changed in AKO mice. We found no measurable differences in adiponectin, leptin, or resistin plasma levels between the WT and AKO (Figures 1M–1O) nor was there any significant difference in levels of C-reactive protein, a global inflammation marker (Figure 1P). In addition, we found no notable difference in plasma TNFα levels as determined by ELISA (Figure 1Q), or in *Tnf* mRNA levels in adipose tissue as quantified by qPCR (Figure 1R).

In addition, we characterized the female mice with the same C57B6/J background at ages 3 months, 6 months, and 12 months. The female mice also exhibited increased adiposity (Figure S1A) and lower blood glucose in OGTT (Figure S1B). We saw no difference in fasting blood glucose until age 12 months where AKO females had lower blood glucose because of higher basal adipose tissue glucose uptake. Other metabolic phenotypes of these female mice were similar to those seen in the male AKO mice including higher fasting FFA and TAG levels, but similar cholesterol levels at age 6 months (Figures S1C and S1D).

Overall, AKO mice possessed modestly expanded adipose tissue because of the conversion of excess glucose into fat for storage in adipose tissue, but they did not show signs of glucose intolerance or global inflammation. These traits make AKO animals a good tool to investigate adipose tissue adaptation during early expansion, without the added complications that accompany an HFD.

AKO mice have increased macrophage numbers in eWAT

We next analyzed the macrophages in epididymal adipose tissue (eWAT) of the WT and AKO mice. Macrophages make up the major immune cell type in eWAT and serve to amplify inflammatory signals. In obese mice, macrophage numbers in eWAT increase.[2] We identified the eWAT macrophages as $CD45^+$, $F4/80^+$, $CD11b^+$, and $CD64^+$ cells from the stromal vascular fraction (SVF) (Figure 2A).[2] We refer to these cells as adipose tissue macrophages (ATM). We also checked for expression of M1-like markers on ATMs, CD9 and CD11c, as well as M2-like marker CD206. For a positive control, we tested wild type C57B6/J male mice fed HFD for 5 weeks and 12 weeks. As expected, after 5 weeks of HFD feeding, mice already had

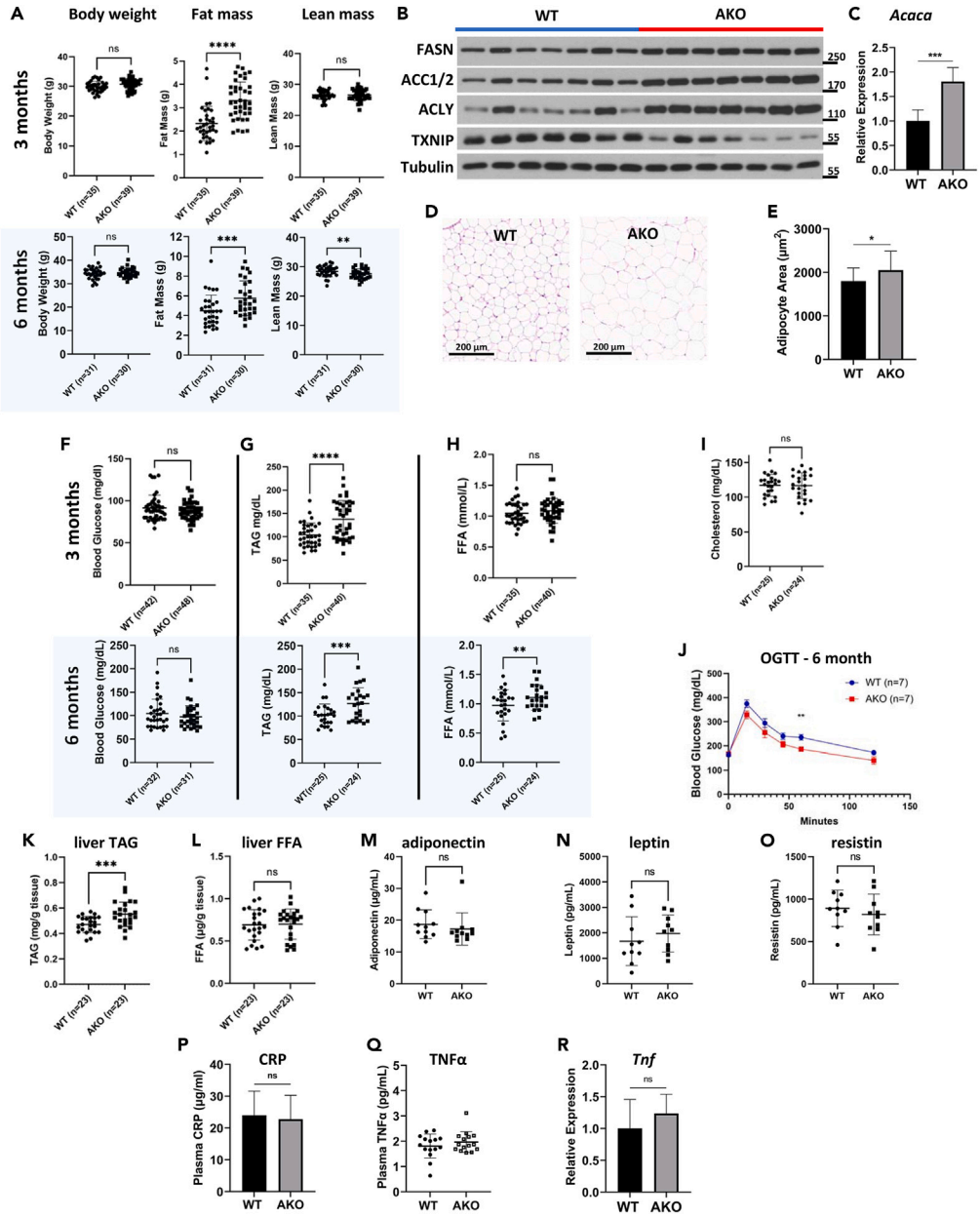

Figure 1. AKO mice are modestly obese without global inflammation on normal diet

(A) Body weight, fat mass and lean mass of WT and AKO male littermates at 3 months and 6 months, as measured by EchoMRI.

(B) Western blots of eWAT at 6 months.

(C) qPCR quantification of eWAT *acaca* mRNA at 6 months (n = 7).

(D) Representative hematoxylin and eosin (H&E) staining of eWAT at 6 months.

(E) Quantification of adipocyte size from H&E (n = 7).

(F–H) Fasting blood glucose, (G) fasting TAG, and (H) fasting FFA of 3-month and 6-month-old WT and AKO male littermates.

(I) Fasting blood cholesterol of 6-month-old WT and AKO male littermates.

(J) OGTT of 6-month-old WT and AKO male littermates.

(K and L) Liver TAG content and (L) FFA content of 6-month-old WT and AKO male littermates.

(M and O) Plasma adiponectin, (N) leptin, (O) resistin content of 6-month-old WT and AKO male littermates.

(P and Q) CRP, and (Q) TNFα of 6-month-old WT and AKO male littermates (n = 10).

Figure 1. *Continued*
(R) eWAT *tnf* mRNA of 6-month-old WT and AKO male littermates (n = 7). (Data presented as mean ± SD. p values calculated with unpaired two-tailed Student's *t* test. *** means $p < 0.001$, ** means $0.001 < p < 0.01$, and * means $0.01 < p < 0.05$.) (Also see Figure S1).

higher body weight, tissue fat content, blood glucose, and FFA levels, but they did not have higher TAG levels (Figure S2A). Hematoxylin and eosin (H&E) staining of eWAT from HFD fed mice showed increased numbers of crown-like structures from mice on HFD compared to mice on a normal diet (Figure S2B), indicating that the eWAT from these mice were inflamed. The FACS results showed an increase in the percentage and number of ATM in the eWAT of these mice, as well as increases in $CD9^+$ and $CD11c^+$ and a decrease in $CD206^+$ ATM populations (Figures S2C and S2D), confirming the inflammatory phenotype of ATMs in these mice. These results showed that the FACS panel worked as intended.

We applied the same panel of markers to 3-month and 6-month-old males as well as to 6-month and 12-month-old females. Because females were smaller than the same-age males, we checked the females at later ages to ensure that there were enough SVF to perform FACS with confidence. In all cases, there was no difference in the number of $CD45^+$ immune cells between the WT and AKO mice (Figures 2B, 2C, S2E, and S2F, left most 2 panels). In males, we saw a trend of increased ATMs in eWAT at age 3 months (Figure 2B), which was significant at 6 months (Figure 2C). We found an increase in the percentage of $CD9^+$ ATMs, however, no difference in $CD11c^+$ M1-like or $CD206^+$ M2-like ATMs. In female eWAT (paraovarian), we saw a significant increase in ATMs only at age 12 months (Figures S3A and S3B). Comparing the males and females, females developed more ATMs at an older age than males, consistent with the literature.[17] Subcutaneous WAT (sWAT) showed no difference in ATMs accumulation or expression markers for either sex (Figure S4), which is also consistent with the literature. Therefore, from FACS data, increased adiposity in AKO is accompanied by increased ATMs in eWAT.

$CD9^+$ ATMs have been reported to be lipid-laden and proinflammatory.[18] CD9 is a member of the tetraspanin superfamily and is widely expressed. It is known to interact with other membrane proteins such as integrins, clustering them into tetraspanin-enriched microdomains to regulate cell-cell adhesion, migration and signal transduction.[19–25] We did not directly measure lipid content in $CD9^+$ ATMs. However, by comparing CD9 gating of 6-month-old WT and AKO males (Figure S5A) to those of control and 5 weeks HFD mice (Figure S5B), it was clear that increase in CD9 surface presentation in AKO ATMs was a lot less than the ATMs from HFD mice. Therefore, the increase in $CD9^+$ in ATMs in AKO indicates changes in ATMs responding to bigger adipocytes, but not necessarily full activation. In addition, other markers of inflammation, including $CD11c^+$ ATM and plasma levels of inflammatory cytokines MCP-1 and IL6 did not show any difference between WT and AKO (Figures 2D and 2E). From these results, it appears that increased $CD9^+$ ATMs can happen early in modest increase in adiposity, without a concomitant increase in other inflammatory markers.

Because only a limited number of markers could be detected by FACS, we decided to look at gene expression of ATMs by mRNAseq. FACS results showed that $CD64^+$ cells were all $CD11b^+$ and $F4/80^+$ (Figure S5C); therefore, we isolated ATMs using anti-CD64 antibody-conjugated magnetic beads from the SVF of 6 pairs of WT and AKO mice. We avoided using FACS for a cleaner population to minimize a further decrease in transcriptional signal and RNA integrity after collagenase digest. Compared to the total eWAT mRNA-seq results from WT and AKO (which will be discussed later), ATM mRNA segregate into different clusters (Figure S6) and which are enriched in macrophage gene expression such as *IL1b*, *Ccl2*(MCP-1), *Tnf*, *IL6*, and *Cxcl2*, and depleted in adipocyte gene expression such as *Adipoq*, *Lep*, and *Fasn* (Figure 2F) indicating enrichment of ATM population. We did not detect increases in the CD9 mRNA level, implying that the differential surface expression of CD9 could be a protein localization adaptation at this point. As shown in a volcano plot, we did not see many significant gene expression differences between the two genotypes (Figure 2G, Table S1). Together, these results demonstrate that early adipose tissue expansion is associated with increase in ATM number, but not by significant ATM inflammatory characteristics.

Ketogenic diet rescues the increase in macrophage number but causes macrophage activation

In addition to regulating glucose uptake, TXNIP protein has other functions yet to be clearly defined. To separate out the glucose-dependent effects from other TXNIP-dependent effects, we put 6-month-old male WT and AKO mice on a ketogenic diet. This diet drives lipid oxidation for energy usage and reduces

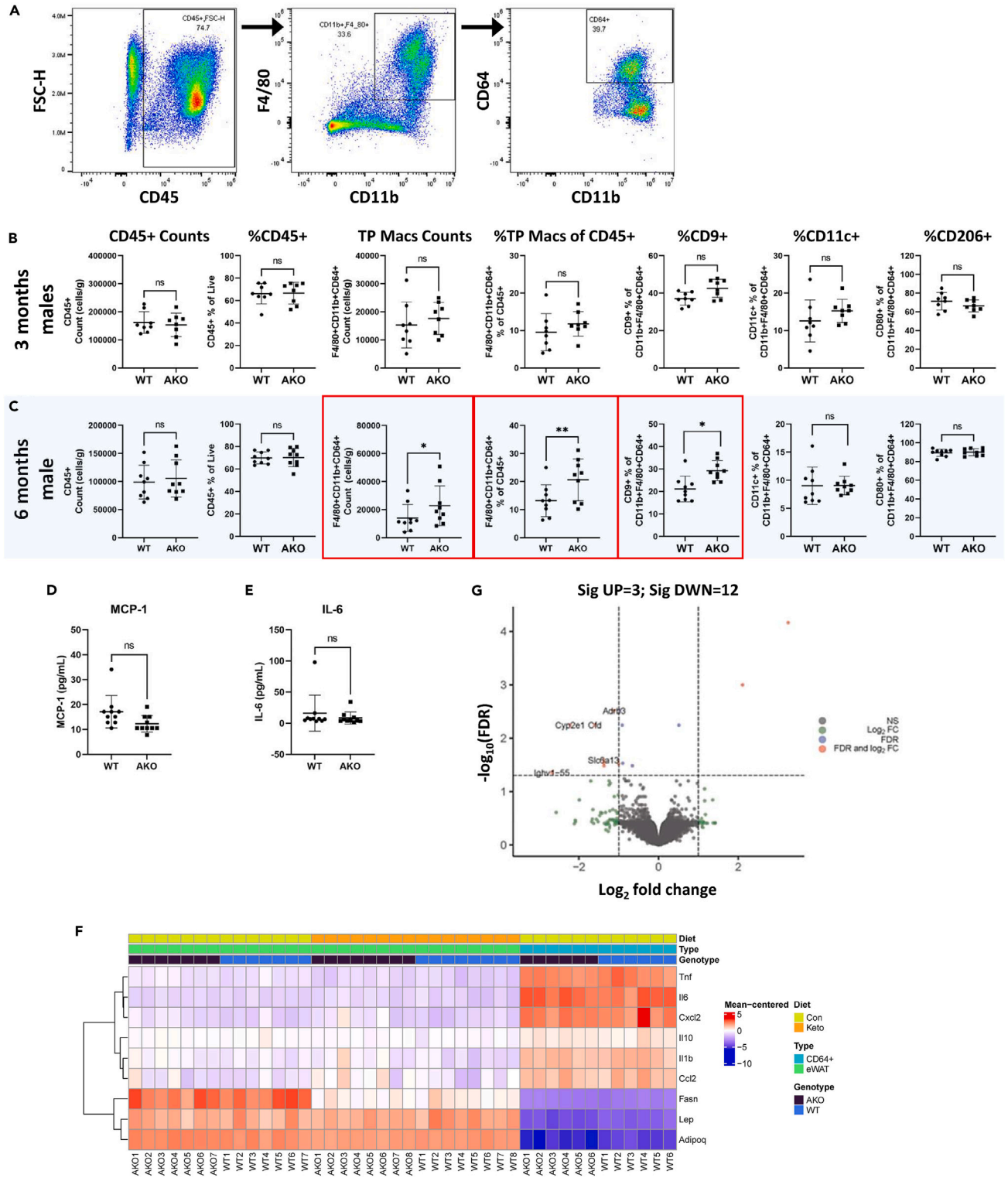

Figure 2. AKO mice have increased number of macrophages on normal diet

(A) Gating scheme for F4/80$^+$, CD11b$^+$ and CD64$^+$ macrophages.

(B and C) ATM FACS results from eWAT of 3-month-old and (C) 6-month-old WT and AKO male littermates.

(D and E) MCP-1 and (E) IL-6 of 6 months WT and AKO male littermates.

Figure 2. *Continued*

(F) Heatmap of expression levels of adipocytes and macrophage marker genes of 6-month-old males.

(G) Volcano plot of differential gene expression between WT and AKO ATMs. (Data presented as mean ± SD. p values calculated with unpaired two-tailed Student's *t* test. *** means $p < 0.001$, ** means $0.001 < p < 0.01$, and * means $0.01 < p < 0.05$.) (Also see Figures S2, S5, and S6, Tables S1, S3, and S4).

glucose consumption in most cells in the body, effectively reducing the glucose uptake difference between WT and AKO adipocytes. Therefore, this diet should minimize the glucose-dependent effects of TXNIP deletion. To prevent complications from excess calorie intake, the mice were given equivalent calorie amounts of the ketogenic diet as their normal chow daily. After three weeks, not only was the fat content of AKO mice the same as that of the control mice, but plasma FFA and TAG levels were also equalized (Figures 3A–3F). Adipocyte size in AKO mice was also similar to that of WT mice after 3 weeks on the ketogenic diet, as seen by H&E staining (Figures 3G and 3H). Lipogenesis decreased in mice on the ketogenic diet as shown by decreased mRNA levels of *Acaca* (Figure 3I). At the same time, mRNA of *Ffar2*, a G-protein coupled receptor for the short chain fatty acids, increased (Figure S7A), indicating increased lipid usage. Fed insulin levels were the same between WT and AKO, but both were lower compared to animals on control chow, as expected (Figure 3J). Thus, the ketogenic diet reduces the metabolic difference observed before between WT and AKO animals.

The ketogenic diet also partially reduced the increase in ATM in AKO. On the ketogenic diet, there was no longer a significant difference in ATM between the WT and AKO eWAT (Figure 3K), indicating that the increased ATMs seen in AKO mice on normal chow is specifically because of increased glucose uptake into the adipocytes. In fact, the ketogenic diet reduced the total number of immune cells ($CD45^+$, 99 K vs. 72 K average per gram of tissue of both genotypes) as well as ATM numbers (14K vs. 5.7K average) in eWAT. However, not only did we continue to see increased $CD9^+$ ATMs, we also found an increase in $CD11c^+$ ATMs and a trend of decreased $CD206^+$ ATMs. These results suggest that after a short period of a ketogenic diet, AKO ATMs exhibit a more proinflammatory phenotype than WT ATMs.

AKO ATMs' proinflammatory properties were further corroborated by higher levels of MCP-1 in the plasma of AKO mice on the ketogenic diet, even though the diet itself tended to lower MCP-1 levels in WT animals compared to the normal chow (Figure 3L). In addition, TNFα levels were lowered by the ketogenic diet in WT but not significantly in AKO animals (Figure 3M). At the same time, IL6, IL1α, IL1β, IL4, IL10, IFNγ, G-CSF, and M-CSF levels remained largely unchanged (Figures S7B–S7I). This suggests that MCP-1 and TNFα are early markers in response to metabolic changes.

Because the metabolic disturbance originated from adipocytes, we therefore measured the plasma concentration of several adipokines. The ketogenic diet tended to increase adiponectin, leptin, and resistin levels compared to the normal diet (Figures 3N–3P). However, only adiponectin showed a significant difference between WT and AKO. AKO did not upregulate adiponectin, in response to the ketogenic diet, to the same extent as WT animals. Adiponectin is well known for its anti-inflammatory properties, and obese people are known to have lower plasma adiponectin levels.[26–28] This trend appears to be captured in AKO mice. Because adiponectin is mainly produced by adipocytes and since macrophage changes are because of signals from adipocytes, the lower level of adiponectin is likely an important reason for the ATM pro-inflammatory phenotype in AKO on the ketogenic diet.

We isolated $CD64^+$ cells from WT and AKO mice on the ketogenic diet and carried out mRNA-seq analysis as before. Heatmap analysis showed enrichment of macrophage genes as seen previously (Figure S7J). We identified 7 genes with significant differential expression between WT and AKO (FDR <0.05) (Figure 3Q), all of which have less expression in AKO. Five of these genes have been reported to suppress inflammation. EGLN1, commonly known as PHD2, is a proline hydroxylase that catalyze the hydroxylation of HIFs (hypoxia-inducible factor), initiating HIF degradation. The myeloid-specific deletion of EGLN1 leads to the exaggerated inflammatory response of neutrophils to *Streptococcus pneumonia*.[29,30] LILRB4, leukocyte immunoglobulin-like receptor B4, is an inhibitory receptor on macrophages that prevents excessive inflammation.[31] LGALS3 (galectin-3) is a galactose-specific lectin that regulates macrophage adhesion and migration. Loss of LGALS3 results in increased expression of proinflammatory genes.[32] GPNMB, glycoprotein non-metastatic melanoma protein b, is highly expressed in macrophages and contributes to resolution of inflammation as it promotes M2 polarization.[33,34] ATP6V0D2 is a subunit of integral membrane V0 complex of vacuolar ATPase which acidifies lysosomes. In macrophages, ATP6V0D2 has been reported to restrict inflammasome activation and promote resolution of inflammation by regulating pro-resolving

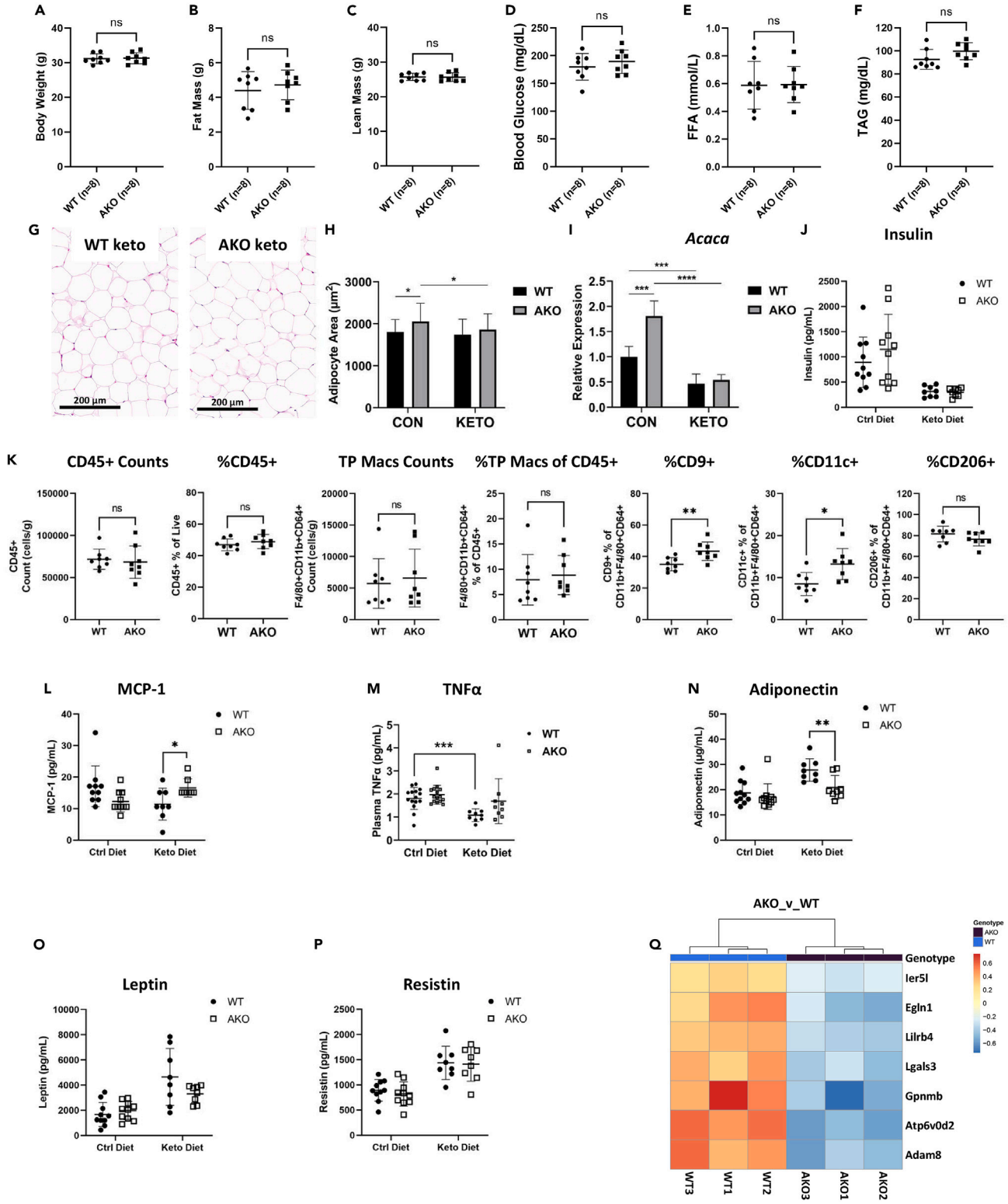

Figure 3. AKO eWAT macrophages become activated after ketogenic diet

(A–F) Body weight, (B) fat mass, (C) lean mass, (D) blood glucose, (E) FFA, and (F) TAG of 6-month-old WT and AKO males following 3 weeks on a ketogenic diet.

(G) H&E staining of eWAT from WT and AKO mice after ketogenic diet.

(H) Adipocyte size quantification of WT and AKO mice before and after ketogenic diet.

Figure 3. *Continued*
(I) qPCR of *acaca* mRNA in eWAT of WT and AKO mice before and after ketogenic diet.
(J) Insulin of WT and AKO mice before and after ketogenic diet.
(K) eWAT macrophage FACS results of WT and AKO mice after ketogenic diet.
(L–P) Plasma MCP-1, (M) TNFα, (N) adiponectin, (O) leptin, and (P) resistin of WT and AKO mice before and after ketogenic diet.
(Q) Heatmap of differentially expressed genes between WT and AKO macrophages after ketogenic diet (FDR <0.05). (Data presented as mean ± SD. Unpaired two-tailed Student's *t* test for calculating p-values for pairwise comparisons and ordinary one-way ANOVA multiple comparisons test for more than 2 groups. *** means $p < 0.001$, ** means $0.001 < p < 0.01$, and * means $0.01 < p < 0.05$.) (Also see Figure S7).

mediators.[35,36] Of the last two genes, not much is known about IER5L (immediate-early response gene 5 like). However, ADAM8 is a metalloproteinase that promotes cell migration,[37,38] which may play a role in why there were less macrophages in the eWAT of mice on the ketogenic diet. The suppression of anti-inflammation genes indicates that before and during the upregulation of proinflammatory response in AKO eWAT, the anti-inflammatory mechanisms have to be turned off. Even though we did not detect any increased mRNA of genes driving inflammation, the reduced expression of anti-inflammatory genes is strong evidence that these AKO ATMs are more proinflammatory than those of WT.

In summary, the ketogenic diet reduced the number of ATMs in AKO eWAT to similar level as WT, indicating that the increased ATMs in eWAT in AKO on the normal diet is a specific effect related to excess-glucose uptake in adipocytes. Surprisingly, the ketogenic diet led to more proinflammatory characteristics in AKO ATMs, as shown by decreased inflammation suppressor gene expression, increased cell surface CD11c, and higher plasma MCP-1 levels. This shift in ATM characteristics is not because of FFA levels, which were similar between WT and AKO on the ketogenic diet. Rather, it correlates with the lower adiponectin levels in AKO.

Increased glucose uptake causes multiple changes in eWAT gene expression

Because we were interested in changes in adipocytes, themselves, we carried out whole tissue mRNA-seq analysis on eWAT. Even though adipose tissue contains multiple cell types, we wanted to avoid the stressful tissue digest which is needed for isolation of a pure adipocyte population. Principal component analysis showed nice separation of groups by diet (Figure S8A). The separation between WT and AKO genotypes was more obvious on control chow than on the ketogenic diet, consistent with metabolic observations so far. We found 2265 significantly (FDR <0.05) differentially expressed (DE) genes on normal diet (Figure 4A) and 884 DE genes on ketogenic diet (Figure 4B). The top changes are listed in Table S2. *Arg1* showed the largest fold increase in mRNA in AKO on the ketogenic diet (more discussion below). To focus on the DE genes response to glucose uptake, we performed clustering analysis according to gene expression profiles (Figure 4C, Table S3) followed by biological process (GO-BP) pathway analysis of each cluster (Figure 4D, Table S4). The mean gene expression of each cluster was plotted in Figure S8B.

Cluster 1 consisted of genes with decreased expression on the ketogenic diet in WT, but not in AKO mice. Many genes in this cluster are involved in immune cell function, including *Arg1*. Because *Arg1* is not expressed in adipocytes (BioGPS, and the Human Protein Atlas), and we did not find it differentially expressed in ATMs, it remains unclear what cell type(s) was responsible for this change. ARG1 is usually considered a marker for M2-like macrophages and it is thought that ARG1 competes with NOS for substrate arginine, thereby decreasing NO production by NOS and reducing inflammation. However, ARG1 has also been shown to be dynamically regulated by HFD, increasing in eWAT after 4-day HFD feeding but disappearing after 2 weeks HFD.[39] Like HFD, the ketogenic diet also has a complex impact on the immune system in a time-dependent manner.[40] Further investigation is required to understand the role that ARG1 is playing in this system.

Cluster 2 contained genes with higher expression in AKO on the normal diet. Not surprisingly, these included genes involved in glucose or sugar metabolism, such as *Acaca* (ACC1), because more glucose was taken up in AKO adipocytes. Of interest, it also included *Hsd11b1*, the corticosteroid 11-β-dehydrogenase that generates ligands for glucocorticoid receptor (GR), suggesting an influence of glucose on GR function.

Cluster 3 genes showed a large difference between the two diets in WT mice and is almost the opposite of cluster 1. It includes genes involved in various types of RNA processing. This is understandable because glucose availability directly affects ribose levels. With less glucose available, the cell must upregulate pathways to efficiently shuttle ribose/RNA to where they are needed the most.

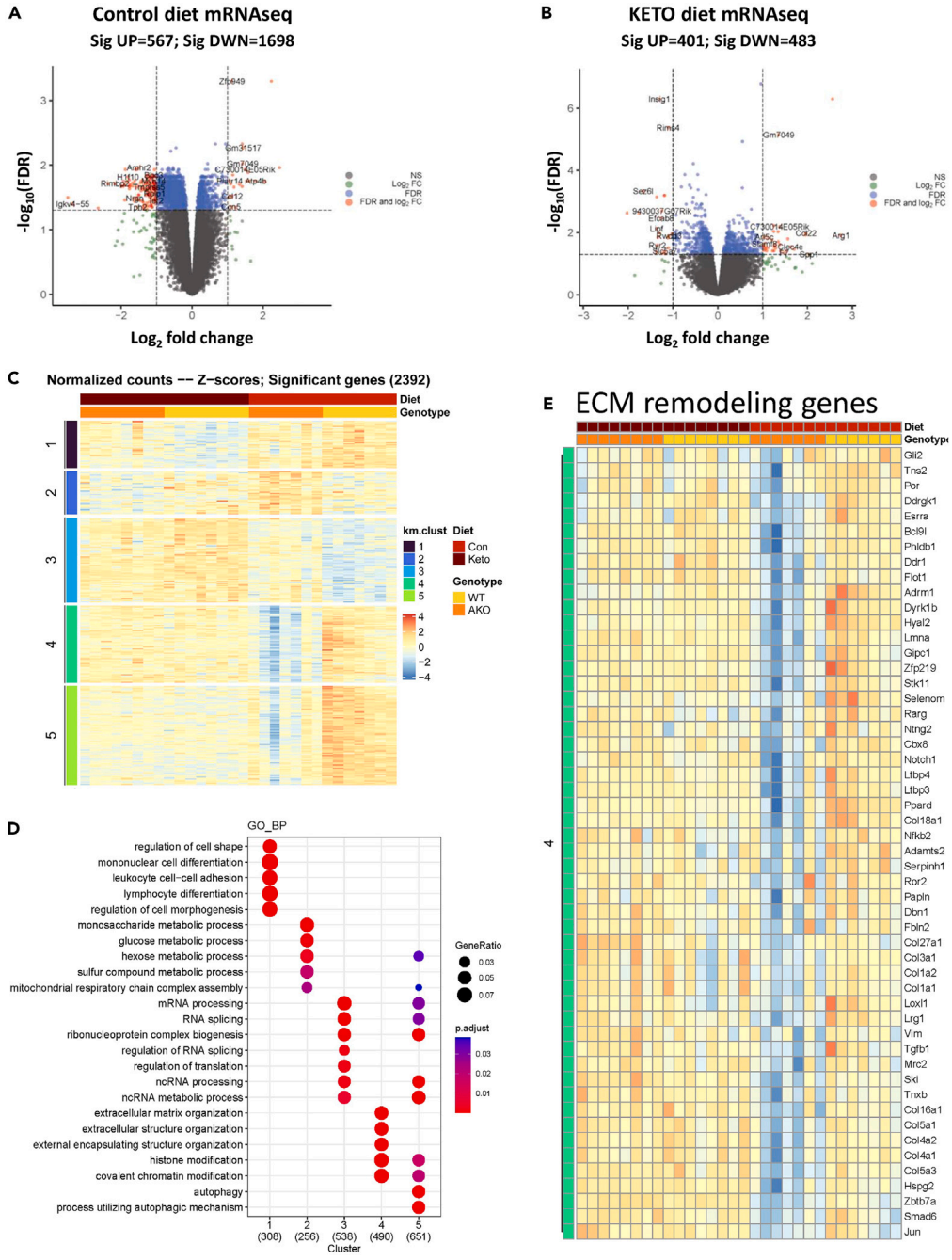

Figure 4. WT and AKO eWAT mRNAseq comparison between normal diet and ketogenic diet

(A) Volcano plot of differentially expressed genes between 6-month-old WT and AKO males on the normal diet.

(B) Volcano plot of differentially expressed genes between 6-month-old WT and AKO males after 3 weeks of ketogenic diet.

(C) Heatmap of clustering analysis between the normal diet and the ketogenic diet.

(D) Pathway analysis of the gene clusters in (C).

(E) Heatmap of genes involved in extracellular matrix (ECM) remodeling in cluster 4. (Also see Figure S8, Tables S2, S3, and S4).

Clusters 4 and 5 were our main interest. They represented glucose-regulated genes, with lower expression in AKO than WT on the normal diet, but with similar expression between the two genotypes on the ketogenic diet. In particular, the extracellular matrix (ECM) organization pathways in cluster 4 drew our attention. The main protein components of adipose ECM are collagens, fibronectin, and laminin.[41–43] These proteins are modified post-translationally and crosslink to provide binding sites for integrins and mechanical support for cells. ECM is remodeled constantly by metalloproteases and this remodeling is important for adipose tissue adaptation to metabolic status. Initial expansion of adipocytes requires increased ECM flexibility to allow more space for adipocyte growth.[44] Later stages of obesity are correlated with increased collagen production and rigidification and fibrosis of the tissue. Examining the genes in pathways involved in ECM remodeling (Figure 4E), we found that expression of collagen genes was repressed (including the major collagen type I and IV), a result that we confirmed at the protein level by quantification of hydroxyproline content (Figure S8C). Other genes with decreased expression included genes involved in collagen biosynthesis (*Serpinh1*, *Vim*, *Loxl1*) and direct ECM genes: tenascin (*Tns2*, *Tnxb*), fibulin (*Fbln2*), heparan sulfate proteoglycan core protein (*Hspg2*), hyaluronidase (*Hyal2*), and proteases (*Adamts2*, *Papln*). Another gene found in cluster 4 was *Tgfb1*, which encodes TGFβ, a potent fibrogenic cytokine[45] that induces ECM production in 3T3L1 cells.[46] Along with *Tgfb1*, we also found genes in cluster 4 that modulate the TGFβ signaling pathway: transcription regulator *Bcl9l*,[47] extracellular glycoprotein *Irg1*,[48,49] and the latent TGFβ binding protein *Itbp3/4*.[50] Thus, AKO adipocytes show decreased ECM production, as well as down regulation of ECM-related regulatory pathways.

Even though lower collagen ECM in AKO eWAT was consistent with its metabolic state of early expanding adipose tissue, overall gene expression changes showed a dynamic and complex adaptation of adipose tissue to increased glucose influx. In clusters 4 and 5, we noticed a reduction in expression of mitochondrial electron transport chain genes as well as mitochondrial ribosomal genes in AKO mice (Figure S8D). In addition, many transcription factors that are important for metabolic regulation, such as *Esrra*, *Ppard*, *Srebf1/2*, *Klf15*, and *Rxra/b* were also included in these two clusters (Figure S8E). ERRα (*Esrra*) is known to regulate many aspects of mitochondrial activity[51]; its decrease implies diminished metabolic reliance on mitochondria by adipocytes. Therefore, not all changes in gene expression because of excess glucose reflected positively on adipocyte health. Altogether, mRNA-seq data showed multifaceted adipocyte adaptations, including ECM reduction in support of increased numbers of ATMs.

DISCUSSION

Many studies have previously demonstrated the significant contribution of ATMs to subclinical inflammation in obesity. Still, the precise signals and mechanisms that lead to the initial ATM migration and/or local activation remain unclear. Identifying these signals and mechanism should help with early diagnosis and prevention of obesity-induced inflammation. Here, we knocked out TXNIP in adipocytes to induce excess glucose uptake by these cells, generating a mouse model exhibiting increased adiposity, but no global inflammation or reduced insulin response. We utilized this model (1) to investigate what happens at the early stages of adipose tissue expansion and (2) to differentiate effects because of glucose from those because of lipids. Throughout these experiments, our goal was to identify factors from adipocytes, themselves, whereas monitoring ATM behavior as a readout.

We learned that increased ATM numbers within eWAT is the most sensitive measure for early adipose tissue expansion and that this is associated with multifaceted adipocyte adjustments, including increased lipolysis and remodeling of ECM. Increased lipolysis and higher levels of TAG in plasma and liver in AKO mice indicate that adipocytes were turning on mechanisms to decrease their TAG storage because they could not effectively turn off basal glucose uptake. Clearly, even though adipocytes are designated as storage tissues, there is an optimal amount of TAG an adipocyte prefers to hold. FFA is a candidate molecular signal for macrophages because of its increase in AKO and its rescue by the ketogenic diet. FFA has been reported to recruit macrophages even during weight loss.[52] Although TAG was also higher in AKO, it is not likely the trigger for ATMs because mice with increased ATM numbers on HFD for 5 weeks did not exhibit higher TAG levels than their control counterparts. Changes in plasma FFA and TAG levels were accompanied by numerous transcriptional changes in eWAT, where ECM remodeling stood out as a potential contributing factor for ATM number increase. In addition to the protein components mentioned before, glucose availability can affect glycosylation pattern on proteoglycans and synthesis of hyaluronan, both of which are important components of ECM that influence cell-cell interaction, including for adipocytes and immune cells.[53,54] The cellular changes facilitating adipocyte expansion co-exist with signs of

adipocytes stress, indicating that the adipose tissue is continually adapting to its environment without a specific boundary or obvious molecular markers that indicate the transition from healthy expansion to non-healthy expansion. Particularly relevant to the human health is the fact that all these unfavorable adipose tissue changes happen before significant total body weight increase was detected, suggesting we need better biomarkers other than BMI to improve early health assessment. Interesting future questions are how do adipocytes determine their optimal size and what triggers excess basal lipolysis as adipocytes enlarge?

We used a ketogenic diet to rescue the metabolic phenotypes and reduce the impact of excess glucose to focus on glucose-specific responses. The ketogenic diet lowered the immune cell population in eWAT and reduced the ATM number difference in WT and AKO. This is consistent with published benefits of a short-term ketogenic diet,[55,56] and our result show that TNFα is lower in WT mice on ketogenic diet than normal diet. However, the remaining ATMs in AKO eWAT gained pro-inflammatory characteristics, marked with higher surface CD11c, higher plasma MCP-1, and decreased expression of inflammation inhibitory genes.

Given that short-term ketogenic diet is not proinflammatory, the proinflammatory characteristics in AKO ATMs on a ketogenic diet may be because of AKO adipocytes retaining characteristics from prior excess glucose uptake. These may include the changes in transcription, ECM constituents and their sugar modification, and increase of shorter, more saturated acyl-chains in structural lipids as we reported before.[16] Particularly interesting to note is the lag of adiponectin increase in AKO behind WT on the ketogenic diet. Adiponectin's known anti-inflammatory properties during diet-induced obesity is supported by its up-regulation in WT on the ketogenic diet whereas prior exposure to excess glucose in AKO inhibited this up-regulation. Given adiponectin is predominantly produced by adipocytes, thus regulated by changes in adipocytes, it is most likely a major player in AKO ATMs acquiring proinflammatory characteristics. TXNIP AKO model also allowed us to see that ATM number is not always correlated with the degree of activation, i.e., more ATMs more activation or vice versa. Non-overlapping pathways regulate these two ATM outputs.

In our model, ATMs from 12-month-old AKO males looked similar to those of 6-month-old AKO males without signs of inflammation (data not shown); therefore, excess glucose alone was insufficient to bring about more proinflammatory changes. In other words, neither excess glucose (TXNIP AKO) nor excess lipids (ketogenic diet) alone were considered as true metabolic excess that demands a full inflammatory response. In addition, even though AKO ATMs gained some proinflammatory characteristics after a short ketogenic diet, they were certainly not as proinflammatory as the ATMs in mice fed 5 weeks of HFD. This study not only supports the fact that the proinflammatory responses ATMs are distinct from infection induced inflammation,[57] it highlights a very wide gradient of responses ATMs can have in response to metabolic perturbation.

Overall, we learned that at the early stages of adipocyte expansion, glucose and lipids exert different influences on adipocytes, leading to different ATM responses. The most interesting mechanistic insight is the importance of inhibitory brakes built-in by nature to prevent undesirable immune activation. Perhaps it is equally important to consider reinforcing these brakes, not just quieting the inflammatory signals, when treating unwanted immune activation.

Limitations of the study

In this study, TXNIP adipocytes-specific knockout animals were used to focus on the effect of excess glucose during the early stages of adipocytes expansion. These results provided glimpses into complex and non-uniform regulation by glucose and lipids. However, this model system cannot definitively separate the differential effects partly because of the higher FFA and TAG levels in TXNIP AKO mice. Consequently, the mRNA analysis that focused on the differentially expressed genes between WT and AKO mice that were rescued by the ketogenic diet missed false negatives regarding glucose-regulated genes.

STAR★METHODS

Detailed methods are provided in the online version of this paper and include the following:

- KEY RESOURCES TABLE
- RESOURCE AVAILABILITY
  - Lead contact

SUPPLEMENTAL INFORMATION

Supplemental information can be found online at https://doi.org/10.1016/j.isci.2023.107163.

ACKNOWLEDGMENTS

The authors thank the VAI vivarium staff for maintaining the mice colonies, the VAI Flow Cytometry core for their support, and the VAI genomics core facility for providing excellent facilities and services. NW is supported by R01-GM120129.

AUTHOR CONTRIBUTIONS

N.W. conceived the idea and designed the experiments. T.A. did FACS and Milliplex experiments. K.L. did all bioinformatic analysis. A.N.W. maintained the mice colonies and carried out mice phenotyping experiments. H.G. and C.K. helped with FACS panel design and data analysis. H.D. did qPCR experiments and IHC quantification.

DECLARATION OF INTERESTS

The authors declare no competing interests.

Received: September 29, 2022
Revised: December 5, 2022
Accepted: June 13, 2023
Published: June 19, 2023

REFERENCES

1. Lobstein, T., Brinsden, H., and Neveux, M. (2022). World Obesity Atlas (World Obesity Federations).

2. Russo, L., and Lumeng, C.N. (2018). Properties and functions of adipose tissue macrophages in obesity. Immunology *155*, 407–417. https://doi.org/10.1111/imm.13002.

3. Burl, R.B., Ramseyer, V.D., Rondini, E.A., Pique-Regi, R., Lee, Y.H., and Granneman, J.G. (2018). Deconstructing Adipogenesis Induced by beta3-Adrenergic Receptor Activation with Single-Cell Expression Profiling. Cell Metabol. *28*, 300–309.e4. https://doi.org/10.1016/j.cmet.2018.05.025.

4. Ruggiero, A.D., Key, C.C.C., and Kavanagh, K. (2021). Adipose Tissue Macrophage Polarization in Healthy and Unhealthy Obesity. Front. Nutr. *8*, 625331. https://doi.org/10.3389/fnut.2021.625331.

5. Nakanishi, T., Fukui, H., Wang, X., Nishiumi, S., Yokota, H., Makizaki, Y., Tanaka, Y., Ohno, H., Tomita, T., Oshima, T., and Miwa, H. (2021). Effect of a High-Fat Diet on the Small-Intestinal Environment and Mucosal Integrity in the. Cells *10*, 3168. https://doi.org/10.3390/cells10113168.

6. Rohr, M.W., Narasimhulu, C.A., Rudeski-Rohr, T.A., and Parthasarathy, S. (2020). Negative Effects of a High-Fat Diet on Intestinal Permeability: A Review. Adv. Nutr. *11*, 77–91. https://doi.org/10.1093/advances/nmz061.

7. Batch, J.T., Lamsal, S.P., Adkins, M., Sultan, S., and Ramirez, M.N. (2020). Advantages and Disadvantages of the Ketogenic Diet: A Review Article. Cureus *12*, e9639. https://doi.org/10.7759/cureus.9639.

8. Dowis, K., and Banga, S. (2021). The Potential Health Benefits of the Ketogenic Diet: A Narrative Review. Nutrients *13*, 1654. https://doi.org/10.3390/nu13051654.

9. Wu, N., Zheng, B., Shaywitz, A., Dagon, Y., Tower, C., Bellinger, G., Shen, C.H., Wen, J., Asara, J., McGraw, T.E., et al. (2013). AMPK-dependent degradation of TXNIP upon energy stress leads to enhanced glucose

uptake via GLUT1. Mol. Cell. *49*, 1167–1175. https://doi.org/10.1016/j.molcel.2013.01.035.

10. Patwari, P., Chutkow, W.A., Cummings, K., Verstraeten, V.L.R.M., Lammerding, J., Schreiter, E.R., and Lee, R.T. (2009). Thioredoxin-independent regulation of metabolism by the alpha-arrestin proteins. J. Biol. Chem. *284*, 24996–25003. https://doi.org/10.1074/jbc.M109.018093.

11. Parikh, H., Carlsson, E., Chutkow, W.A., Johansson, L.E., Storgaard, H., Poulsen, P., Saxena, R., Ladd, C., Schulze, P.C., Mazzini, M.J., et al. (2007). TXNIP regulates peripheral glucose metabolism in humans. PLoS Med. *4*, e158. https://doi.org/10.1371/journal.pmed.0040158.

12. Chutkow, W.A., Patwari, P., Yoshioka, J., and Lee, R.T. (2008). Thioredoxin-interacting protein (Txnip) is a critical regulator of hepatic glucose production. J. Biol. Chem. *283*, 2397–2406. https://doi.org/10.1074/jbc.M708169200.

13. Dykstra, H., LaRose, C., Fisk, C., Waldhart, A., Meng, X., Zhao, G., and Wu, N. (2021). TXNIP interaction with GLUT1 depends on PI(4,5)P(2). Biochim. Biophys. Acta, Biomembr. *1863*, 183757. https://doi.org/10.1016/j.bbamem.2021.183757.

14. Waldhart, A.N., Dykstra, H., Peck, A.S., Boguslawski, E.A., Madaj, Z.B., Wen, J., Veldkamp, K., Hollowell, M., Zheng, B., Cantley, L.C., et al. (2017). Phosphorylation of TXNIP by AKT Mediates Acute Influx of Glucose in Response to Insulin. Cell Rep. *19*, 2005–2013. https://doi.org/10.1016/j.celrep.2017.05.041.

15. Chutkow, W.A., Birkenfeld, A.L., Brown, J.D., Lee, H.Y., Frederick, D.W., Yoshioka, J., Patwari, P., Kursawe, R., Cushman, S.W., Plutzky, J., et al. (2010). Deletion of the alpha-arrestin protein Txnip in mice promotes adiposity and adipogenesis while preserving insulin sensitivity. Diabetes *59*, 1424–1434. https://doi.org/10.2337/db09-1212.

16. Waldhart, A.N., Muhire, B., Johnson, B., Pettinga, D., Madaj, Z.B., Wolfrum, E., Dykstra, H., Wegert, V., Pospisilik, J.A., Han, X., and Wu, N. (2021). Excess dietary carbohydrate affects mitochondrial integrity as observed in brown adipose tissue. Cell Rep. *36*, 109488. https://doi.org/10.1016/j.celrep.2021.109488.

17. Palmer, B.F., and Clegg, D.J. (2015). The sexual dimorphism of obesity. Mol. Cell. Endocrinol. *402*, 113–119. https://doi.org/10.1016/j.mce.2014.11.029.

18. Hill, D.A., Lim, H.W., Kim, Y.H., Ho, W.Y., Foong, Y.H., Nelson, V.L., Nguyen, H.C.B., Chegireddy, K., Kim, J., Habertheuer, A., et al. (2018). Distinct macrophage populations direct inflammatory versus physiological changes in adipose tissue. Proc. Natl. Acad. Sci. USA *115*, E5096–E5105. https://doi.org/10.1073/pnas.1802611115.

19. Brosseau, C., Colas, L., Magnan, A., and Brouard, S. (2018). CD9 Tetraspanin: A New Pathway for the Regulation of Inflammation? Front. Immunol. *9*, 2316. https://doi.org/10.3389/fimmu.2018.02316.

20. Reyes, R., Cardeñes, B., Machado-Pineda, Y., and Cabañas, C. (2018). Tetraspanin CD9: A Key Regulator of Cell Adhesion in the Immune System. Front. Immunol. *9*, 863. https://doi.org/10.3389/fimmu.2018.00863.

21. Wang, H.X., and Hemler, M.E. (2015). Novel impact of EWI-2, CD9, and CD81 on TGF-beta signaling in melanoma. Mol. Cell. Oncol. *2*, e1030536. https://doi.org/10.1080/23723556.2015.1030536.

22. Lazareth, H., Henique, C., Lenoir, O., Puelles, V.G., Flamant, M., Bollée, G., Fligny, C., Camus, M., Guyonnet, L., Millien, C., et al. (2019). The tetraspanin CD9 controls migration and proliferation of parietal epithelial cells and glomerular disease progression. Nat. Commun. *10*, 3303. https://doi.org/10.1038/s41467-019-11013-2.

23. Herr, M.J., Mabry, S.E., and Jennings, L.K. (2014). Tetraspanin CD9 regulates cell contraction and actin arrangement via RhoA in human vascular smooth muscle cells. PLoS One *9*, e106999. https://doi.org/10.1371/journal.pone.0106999.

24. Charrin, S., Jouannet, S., Boucheix, C., and Rubinstein, E. (2014). Tetraspanins at a glance. J. Cell Sci. *127*, 3641–3648. https://doi.org/10.1242/jcs.154906.

25. Hemler, M.E. (2014). Tetraspanin proteins promote multiple cancer stages. Nat. Rev. Cancer *14*, 49–60. https://doi.org/10.1038/nrc3640.

26. Achari, A.E., and Jain, S.K. (2017). Adiponectin, a Therapeutic Target for Obesity, Diabetes, and Endothelial Dysfunction. Int. J. Mol. Sci. *18*, 1321. https://doi.org/10.3390/ijms18061321.

27. Luo, Y., and Liu, M. (2016). Adiponectin: a versatile player of innate immunity. J. Mol. Cell Biol. *8*, 120–128. https://doi.org/10.1093/jmcb/mjw012.

28. Ohashi, K., Parker, J.L., Ouchi, N., Higuchi, A., Vita, J.A., Gokce, N., Pedersen, A.A., Kalthoff, C., Tullin, S., Sams, A., et al. (2010). Adiponectin promotes macrophage polarization toward an anti-inflammatory phenotype. J. Biol. Chem. *285*, 6153–6160. https://doi.org/10.1074/jbc.M109.088708.

29. Muz, B., Larsen, H., Madden, L., Kiriakidis, S., and Paleolog, E.M. (2012). Prolyl hydroxylase domain enzyme 2 is the major player in regulating hypoxic responses in rheumatoid arthritis. Arthritis Rheum. *64*, 2856–2867. https://doi.org/10.1002/art.34479.

30. Watts, E.R., and Walmsley, S.R. (2019). Inflammation and Hypoxia: HIF and PHD Isoform Selectivity. Trends Mol. Med. *25*, 33–46. https://doi.org/10.1016/j.molmed.2018.10.006.

31. Mitsune, A., Yamada, M., Fujino, N., Numakura, T., Ichikawa, T., Suzuki, A., Matsumoto, S., Mitsuhashi, Y., Itakura, K., Makiguchi, T., et al. (2021). Upregulation of leukocyte immunoglobulin-like receptor B4 on interstitial macrophages in COPD; their possible protective role against emphysema formation. Respir. Res. *22*, 232. https://doi.org/10.1186/s12931-021-01828-3.

32. Di Gregoli, K., Somerville, M., Bianco, R., Thomas, A.C., Frankow, A., Newby, A.C., George, S.J., Jackson, C.L., and Johnson, J.L. (2020). Galectin-3 Identifies a Subset of Macrophages With a Potential Beneficial Role in Atherosclerosis. Arterioscler. Thromb. Vasc. Biol. *40*, 1491–1509. https://doi.org/10.1161/ATVBAHA.120.314252.

33. Saade, M., Araujo de Souza, G., Scavone, C., and Kinoshita, P.F. (2021). The Role of GPNMB in Inflammation. Front. Immunol. *12*, 674739. https://doi.org/10.3389/fimmu.2021.674739.

34. Zhou, L., Zhuo, H., Ouyang, H., Liu, Y., Yuan, F., Sun, L., Liu, F., and Liu, H. (2017). Glycoprotein non-metastatic melanoma protein b (Gpnmb) is highly expressed in macrophages of acute injured kidney and promotes M2 macrophages polarization. Cell. Immunol. *316*, 53–60. https://doi.org/10.1016/j.cellimm.2017.03.006.

35. Rao, Z., Pace, S., Jordan, P.M., Bilancia, R., Troisi, F., Börner, F., Andreas, N., Kamradt, T., Menche, D., Rossi, A., et al. (2019). Vacuolar (H(+))-ATPase Critically Regulates Specialized Proresolving Mediator Pathways in Human M2-like Monocyte-Derived Macrophages and Has a Crucial Role in Resolution of Inflammation. J. Immunol. *203*, 1031–1043. https://doi.org/10.4049/jimmunol.1900236.

36. Xia, Y., Liu, N., Xie, X., Bi, G., Ba, H., Li, L., Zhang, J., Deng, X., Yao, Y., Tang, Z., et al. (2019). The macrophage-specific V-ATPase subunit ATP6V0D2 restricts inflammasome activation and bacterial infection by facilitating autophagosome-lysosome fusion. Autophagy *15*, 960–975. https://doi.org/10.1080/15548627.2019.1569916.

37. Dreymueller, D., Pruessmeyer, J., Schumacher, J., Fellendorf, S., Hess, F.M., Seifert, A., Babendreyer, A., Bartsch, J.W., and Ludwig, A. (2017). The metalloproteinase ADAM8 promotes leukocyte recruitment in vitro and in acute lung inflammation. Am. J. Physiol. Lung Cell Mol. Physiol. *313*, L602–L614. https://doi.org/10.1152/ajplung.00444.2016.

38. Puolakkainen, P., Koski, A., Vainionpää, S., Shen, Z., Repo, H., Kemppainen, E., Mustonen, H., and Seppänen, H. (2014). Anti-inflammatory macrophages activate invasion in pancreatic adenocarcinoma by increasing the MMP9 and ADAM8 expression. Med. Oncol. *31*, 884. https://doi.org/10.1007/s12032-014-0884-9.

39. Ji, Y., Sun, S., Xia, S., Yang, L., Li, X., and Qi, L. (2012). Short term high fat diet challenge promotes alternative macrophage polarization in adipose tissue via natural killer T cells and interleukin-4. J. Biol. Chem. *287*, 24378–24386. https://doi.org/10.1074/jbc.M112.371807.

40. Goldberg, E.L., Shchukina, I., Asher, J.L., Sidorov, S., Artyomov, M.N., and Dixit, V.D. (2020). Ketogenesis activates metabolically protective gammadelta T cells in visceral

adipose tissue. Nat. Metab. *2*, 50–61. https://doi.org/10.1038/s42255-019-0160-6.

41. Karsdal, M.A., Nielsen, M.J., Sand, J.M., Henriksen, K., Genovese, F., Bay-Jensen, A.C., Smith, V., Adamkewicz, J.I., Christiansen, C., and Leeming, D.J. (2013). Extracellular matrix remodeling: the common denominator in connective tissue diseases. Possibilities for evaluation and current understanding of the matrix as more than a passive architecture, but a key player in tissue failure. Assay Drug Dev. Technol. *11*, 70–92. https://doi.org/10.1089/adt.2012.474.

42. Ruiz-Ojeda, F.J., Méndez-Gutiérrez, A., Aguilera, C.M., and Plaza-Díaz, J. (2019). Extracellular Matrix Remodeling of Adipose Tissue in Obesity and Metabolic Diseases. Int. J. Mol. Sci. *20*, 4888. https://doi.org/10.3390/ijms20194888.

43. Khan, T., Muise, E.S., Iyengar, P., Wang, Z.V., Chandalia, M., Abate, N., Zhang, B.B., Bonaldo, P., Chua, S., and Scherer, P.E. (2009). Metabolic dysregulation and adipose tissue fibrosis: role of collagen VI. Mol. Cell Biol. *29*, 1575–1591. https://doi.org/10.1128/MCB.01300-08.

44. Datta, R., Podolsky, M.J., and Atabai, K. (2018). Fat fibrosis: friend or foe? JCI Insight *3*, e122289. https://doi.org/10.1172/jci.insight.122289.

45. Lee, M.J. (2018). Transforming growth factor beta superfamily regulation of adipose tissue biology in obesity. Biochim. Biophys. Acta, Mol. Basis Dis. *1864*, 1160–1171. https://doi.org/10.1016/j.bbadis.2018.01.025.

46. Gagnon, A.M., Chabot, J., Pardasani, D., and Sorisky, A. (1998). Extracellular matrix induced by TGFbeta impairs insulin signal transduction in 3T3-L1 preadipose cells. J. Cell. Physiol. *175*, 370–378. https://doi.org/10.1002/(SICI)1097-4652(199806)175:3<370::AID-JCP15>3.0.CO;2-9.

47. Sannino, G., Armbruster, N., Bodenhöfer, M., Haerle, U., Behrens, D., Buchholz, M., Rothbauer, U., Sipos, B., and Schmees, C. (2016). Role of BCL9L in transforming growth factor-beta (TGF-beta)-induced epithelial-to-mesenchymal-transition (EMT) and metastasis of pancreatic cancer. Oncotarget *7*, 73725–73738. https://doi.org/10.18632/oncotarget.12455.

48. Wang, X., Abraham, S., McKenzie, J.A.G., Jeffs, N., Swire, M., Tripathi, V.B., Luhmann, U.F.O., Lange, C.A.K., Zhai, Z., Arthur, H.M., et al. (2013). LRG1 promotes angiogenesis by modulating endothelial TGF-beta signalling. Nature *499*, 306–311. https://doi.org/10.1038/nature12345.

49. Minchin, J.E.N., Dahlman, I., Harvey, C.J., Mejhert, N., Singh, M.K., Epstein, J.A., Arner, P., Torres-Vázquez, J., and Rawls, J.F. (2015). Plexin D1 determines body fat distribution by regulating the type V collagen microenvironment in visceral adipose tissue. Proc. Natl. Acad. Sci. USA *112*, 4363–4368. https://doi.org/10.1073/pnas.1416412112.

50. Robertson, I.B., Horiguchi, M., Zilberberg, L., Dabovic, B., Hadjiolova, K., and Rifkin, D.B. (2015). Latent TGF-beta-binding proteins. Matrix Biol. *47*, 44–53. https://doi.org/10.1016/j.matbio.2015.05.005.

51. Tripathi, M., Yen, P.M., and Singh, B.K. (2020). Estrogen-Related Receptor Alpha: An Under-Appreciated Potential Target for the Treatment of Metabolic Diseases. Int. J. Mol. Sci. *21*, 1645. https://doi.org/10.3390/ijms21051645.

52. Kosteli, A., Sugaru, E., Haemmerle, G., Martin, J.F., Lei, J., Zechner, R., and Ferrante, A.W., Jr. (2010). Weight loss and lipolysis promote a dynamic immune response in murine adipose tissue. J. Clin. Invest. *120*, 3466–3479. https://doi.org/10.1172/JCI42845.

53. Pessentheiner, A.R., Ducasa, G.M., and Gordts, P.L.S.M. (2020). Proteoglycans in Obesity-Associated Metabolic Dysfunction and Meta-Inflammation. Front. Immunol. *11*, 769. https://doi.org/10.3389/fimmu.2020.00769.

54. Moretto, P., Karousou, E., Viola, M., Caon, I., D'Angelo, M.L., De Luca, G., Passi, A., and Vigetti, D. (2015). Regulation of hyaluronan synthesis in vascular diseases and diabetes. J. Diabetes Res. *2015*, 167283. https://doi.org/10.1155/2015/167283.

55. Goldberg, E.L., Molony, R.D., Kudo, E., Sidorov, S., Kong, Y., Dixit, V.D., and Iwasaki, A. (2019). Ketogenic diet activates protective gammadelta T cell responses against influenza virus infection. Sci. Immunol. *4*, eaav2026. https://doi.org/10.1126/sciimmunol.aav2026.

56. Crosby, L., Davis, B., Joshi, S., Jardine, M., Paul, J., Neola, M., and Barnard, N.D. (2021). Ketogenic Diets and Chronic Disease: Weighing the Benefits Against the Risks. Front. Nutr. *8*, 702802. https://doi.org/10.3389/fnut.2021.702802.

57. Kratz, M., Coats, B.R., Hisert, K.B., Hagman, D., Mutskov, V., Peris, E., Schoenfelt, K.Q., Kuzma, J.N., Larson, I., Billing, P.S., et al. (2014). Metabolic dysfunction drives a mechanistically distinct proinflammatory phenotype in adipose tissue macrophages. Cell Metabol. *20*, 614–625. https://doi.org/10.1016/j.cmet.2014.08.010.

58. Dobin, A., Davis, C.A., Schlesinger, F., Drenkow, J., Zaleski, C., Jha, S., Batut, P., Chaisson, M., and Gingeras, T.R. (2013). STAR: ultrafast universal RNA-seq aligner. Bioinformatics *29*, 15–21. https://doi.org/10.1093/bioinformatics/bts635.

59. Chen, Y., Lun, A.T.L., and Smyth, G.K. (2016). From reads to genes to pathways: differential expression analysis of RNA-Seq experiments using Rsubread and the edgeR quasi-likelihood pipeline. F1000Res. *5*, 1438. https://doi.org/10.12688/f1000research.8987.2.

60. Robinson, M.D., McCarthy, D.J., and Smyth, G.K. (2010). edgeR: a Bioconductor package for differential expression analysis of digital gene expression data. Bioinformatics *26*, 139–140. https://doi.org/10.1093/bioinformatics/btp616.

61. Love, M.I., Huber, W., and Anders, S. (2014). Moderated estimation of fold change and dispersion for RNA-seq data with DESeq2. Genome Biol. *15*, 550. https://doi.org/10.1186/s13059-014-0550-8.

62. Gu, Z., Eils, R., and Schlesner, M. (2016). Complex heatmaps reveal patterns and correlations in multidimensional genomic data. Bioinformatics *32*, 2847–2849. https://doi.org/10.1093/bioinformatics/btw313.

63. Durinck, S., Spellman, P.T., Birney, E., and Huber, W. (2009). Mapping identifiers for the integration of genomic datasets with the R/Bioconductor package biomaRt. Nat. Protoc. *4*, 1184–1191. https://doi.org/10.1038/nprot.2009.97.

64. Yu, G., Wang, L.G., Han, Y., and He, Q.Y. (2012). clusterProfiler: an R package for comparing biological themes among gene clusters. OMICS *16*, 284–287. https://doi.org/10.1089/omi.2011.0118.

65. Rath, S., Sharma, R., Gupta, R., Ast, T., Chan, C., Durham, T.J., Goodman, R.P., Grabarek, Z., Haas, M.E., Hung, W.H.W., et al. (2021). MitoCarta3.0: an updated mitochondrial proteome now with sub-organelle localization and pathway annotations. Nucleic Acids Res. *49*, D1541–D1547. https://doi.org/10.1093/nar/gkaa1011.

66. Fagerberg, L., Hallström, B.M., Oksvold, P., Kampf, C., Djureinovic, D., Odeberg, J., Habuka, M., Tahmasebpoor, S., Danielsson, A., Edlund, K., et al. (2014). Analysis of the human tissue-specific expression by genome-wide integration of transcriptomics and antibody-based proteomics. Mol. Cell. Proteomics *13*, 397–406. https://doi.org/10.1074/mcp.M113.035600.

STAR★METHODS

KEY RESOURCES TABLE

REAGENT or RESOURCE	SOURCE	IDENTIFIER
Antibodies		
PE-Cy7 anti-mouse Ly-6G, Clone 1A8 (FC, 1:2560)	BioLegend	Cat#127617 RRID:AB_1877262
PE-Cy7 anti-mouse CD3, Clone 17A (FC, 1:2560)	BioLegend	Cat#100219 RRID:AB_1732068
PE-Cy7 anti-mouse CD19, Clone 6D5 (FC, 1:1280)	BioLegend	Cat#115519 RRID:AB_313654
PE-Cy7 anti-mouse NK1.1/CD161, Clone PK136 (FC, 1:640)	BioLegend	Cat#108713 RRID:AB_389363
PE-Cy7 anti-mouse B220/CD45R, Clone RA3-6B2 (FC, 1:2560)	BioLegend	Cat#103221 RRID:AB_313004
BUV395 anti-mouse CD9, Clone KMC8 (FC, 1:20)	BD Biosciences	Cat#740244 RRID:AB_2739991
APC-R700 anti-mouse CD11b, Clone M1/70 (FC, 1:640)	BD Biosciences	Cat#564985 RRID:AB_2739033
Brilliant Violet 421 anti-mouse CD11c, Clone N418 (FC, 1:80)	BioLegend	Cat#117343 RRID:AB_2563099
Alexa Fluor 488 anti-mouse CD36, Clone HM36 (FC, 1:200)	BioLegend	Cat#102608 RRID:AB_528792
Brilliant Violet 786 anti-mouse CD64, Clone X54-5/7.1 (FC, 1:320)	BD Biosciences	Cat#741024 RRID:AB_2740644
PE anti-mouse CD80, Clone 16-10A1 (FC, 1:300)	Invitrogen	Cat#12-0801-82 RRID:AB_465752
APC anti-mouse CD206, Clone C068C2 (FC, 1:1280)	BioLegend	Cat#141707 RRID:AB_10896057
PE-Dazzle 594 anti-mouse F4/80, Clone BM8 (FC, 1:160)	BioLegend	Cat#123145 RRID:AB_2564132
Brilliant Violet 570 anti-mouse Ly-6C, Clone HK1.4 (FC, 1:1280)	BioLegend	Cat#128029 RRID:AB_10896061
BUV805 anti-mouse MHCII, Clone M5/114.15.2 (FC, 1:640)	BD Biosciences	Cat#748844 RRID:AB_2873247
Brilliant Violet 650 anti-mouse XCR1, Clone ZET (FC, 1:3000)	BioLegend	Cat#148220 RRID:AB_2566410
BUV496 anti-mouse CD45, Clone I3/2.3 (FC, 1:100)	BD Biosciences	Cat#752411 RRID:AB_2917425
Fc Block (mAb CD16/CD32)	Invitrogen	Cat#14-0161-86 RRID:AB_467135
Biotinylated anti-CD64	BioLegend	139318 RRID:AB_2566557
Chemicals, peptides, and recombinant proteins		
Zombie Aqua Fixable Viability Dye	BioLegend	Cat#423101
Collagenase II	Worthington	Cat#LS004177
RPMI 1640, 1X, with L-glutamine	Corning	Cat#10-040-CV
FBS	Gibco	Cat#10437-028

(*Continued on next page*)

Continued

REAGENT or RESOURCE	SOURCE	IDENTIFIER
Penicillin-Streptomycin	Gibco	Cat#15140-122
HBSS	Sigma	Cat#H1387-10X1L
BD Horizon Brilliant Stain Buffer	BD Biosciences	Cat#566349
True-Stain Monocyte Blocker	BioLegend	Cat#426103
Ultra-Comp eBeads compensation beads	Invitrogen	Cat#01-2222-42
Ultra Rainbow Fluorescent Particles mid-range intensity beads	Spherotech	Cat#URFP-38-5A
BSA	Sigma	Cat#A4503
16% Formaldehyde Solution	Thermo Scientific	Cat#28906
10X PBS pH 7.4 without $CaCl_2$ or $MgCl_2$	Invitrogen	Cat#70011044
Streptavidin magnetic beads	ThermoFisher	11205D
TRIzol™	ThermoFisher	15596026
SuperScript™ VILO™ Master Mix	ThermoFisher Scientific	11755050
PureLink™ RNA mini kit	ThermoFisher	12183018A
Critical commercial assays		
MILLIPLEX MAP Mouse Adipokine Magnetic Bead Panel - Endocrine Multiplex Assay	Millipore	Cat#MADKMAG-71K
Mouse Adiponectin Single Plex Magnetic Bead Kit	Millipore	Cat# MADPNMAG-70K-01
Mouse Cytokine Magnetic Bead Panel	Millipore	MCYTOMAG-70K
TNFα Quantikine HS ELISA kit	R&D	MHSTA50
Mouse CRP ELISA	Millipore	RAB1121
Total Collagen Assay kit	Abcam	Ab222942
PureLink™ RNA mini kit	ThermoFisher Scientific	12183018A
Infinity Triglyceride kit	ThermoFisher Scientific	TR22421
NEFA-HR2 kit	FujiFilm Wako Pure Chemical Corporation	999-34691, 991-34891, 995-34791, 993-35191, 276-76491
Total cholesterol reagents	ThermoFisher Scientific	TR13421
Qiagen RNeasy Micro kit	Qiagen	74004
Deposited data		
mRNAseq	GEO	GSE212875
Experimental models: Organisms/strains		
Mouse:	The Jackson Laboratory	JAX:
Mouse: B6;129-Txniptm1Rlee/J	The Jackson Laboratory	JAX: 016847
Mouse: B6.FVB-Tg(Adipoq-cre)1Evdr/J	The Jackson Laboratory	JAX: 028020
Software and algorithms		
xPONENT v.4.1	Luminex	https://www.luminexcorp.com/xponent/#overview
Belysa curve-analysis software (version unknown)	Millipore	https://www.sigmaaldrich.com/US/en/services/software-and-digital-platforms/belysa-immunoassay-curve-fitting-software
SpectroFlo v2.1.0	Cytek Biosciences	https://cytekbio.com/pages/spectro-floflow
FlowJo v10.6.2	BD Biosciences	https://www.flowjo.com/
STAR v2.7.8a	Dobin et al.[58]	https://github.com/alexdobin/STAR
edgeR v3.34.1	Chen et al.[59]; Robinson et al.[60]	https://bioconductor.org/packages/release/bioc/html/edgeR.html

(*Continued on next page*)

Continued

REAGENT or RESOURCE	SOURCE	IDENTIFIER
DEseq2 v1.32.0	Love et al.[61]	https://bioconductor.org/packages/release/bioc/html/DESeq2.html
ComplexHeatmap v2.8.0	Gu et al.[62]	https://bioconductor.org/packages/release/bioc/html/ComplexHeatmap.html
biomaRt v2.48.3	Durinck et al.[63]	https://bioconductor.org/packages/release/bioc/html/biomaRt.html
clusterProfiler v4.0.5	Yu et al.[64]	https://bioconductor.org/packages/release/bioc/html/clusterProfiler.html
GraphPad Prism v9.1.1	GraphPad Software	https://www.graphpad.com/

RESOURCE AVAILABILITY

Lead contact

Further information and requests for resources and reagents should be directed to and will be fulfilled by the Lead Contact Ning Wu (ning@omnispacemail.com).

Materials availability

This study did not generate new unique reagents.

Data and code availability

- mRNAseq data generated during this study are available as GEO GSE212875.
- No new code was generated.
- No other new unique reagent was generated.
- Any additional information required to reanalyze the data reported in this paper is available from the lead contact upon request.

EXPERIMENTAL MODEL AND STUDY PARTICIPANT DETAILS

Mice were maintained in a barrier facility, in accord with the Institute's regulations for animal care and handling (IACUC 19-07-021). Strains TXNIP flox/flox (JAX 016847) and Adipoq-Cre (JAX 028020) were purchased from the Jackson Laboratory. The adipose-specific KO mice were backcrossed to C57B6/J (JAX 000664) for over 10 generations. For experiments, sex-matched littermates were used. Mice were maintained on LabDiet 5010 (normal diet, calorie composition: 28.7% from protein, 12.7% from fat, and 58.2% from carbohydrate) unless otherwise stated. Ketogenic diet was purchased from Envigo (TD.96355.PWD, calorie composition: 9.2% from protein, 90.5% from fat, and 0.3% from carbohydrate).

METHOD DETAILS

OGTT

Male littermate matched *Txnip* fl/fl and AdipoQ-Cre Tg/+, *Txnip* fl/fl mice were fasted from 7 a.m. to 1:30 p.m. A bolus of glucose at 2 g/kg was delivered via oral gavage. Blood was sampled via the tail vein at various time points. Blood glucose was measured with Accu-Chek (Aviva).

Lean mass and fat mass were measured with an EchoMRI-4n1-500 system.

FFA, TAG, cholesterol

Tissue TAG was measure with Infinity Triglyceride kit from ThermoFisher Scientific. FFA was measured with NEFA-HR2 kit from FujiFilm. Cholesterol was measured with total cholesterol reagents from ThermoFisher Scientific.

Histology

Tissue was fixed with 4% formaldehyde in PBS for 48h and sent to VAI histology core for embedding. Deparaffinization and antigen retrieval were performed on the Dako PT link platform using Dako High pH retriever buffer for 20 minutes at 97°C. Staining was performed utilizing Dako Autostainer Link 48, and Dako Rabbit Polymer HRP as secondary antibody for 20 minutes following primary antibody incubation for 30 minutes. DAB detection was performed using Dako EnVision Flex Chromagen for 10 minutes and Dako Flex Hematoxylin for 5 minutes. Aperio scanning of slides was performed utilizing Leica Aperio AT2 system.

Western blots

Mice were sacrificed and eWAT was dissected out and frozen immediately in liquid nitrogen and stored at −80°C. Frozen tissues were lysed in RIPA buffer (30 mM Tris7.5, 120 mM NaCl, 1 mM vanadate, 20 mM NaF, 1% NP40, 1% deoxycholate, 0.1% SDS), plus protease inhibitors and calyculin A. The clarified supernatant was used for running Western blots.

TNFα and CRP assays

Plasma TNFα level was measured with mouse TNFα Quantikine HS ELISA from R&D (MHSTA50) according to the manufacturer's instructions. The CRP ELISA was the Mouse CRP ELISA from Millipore-Sigma (#RAB1121).

Milliplex assay

Plasma samples were assayed using the Millipore Milliplex Mouse Adipokine Magnetic Beads Assay kit according to the manufacturer's instructions, with a 6-analyte custom panel investigating IL-6, insulin, leptin, MCP-1, and resistin. Briefly, the analyte-bead mixture was added to adipokine standards, QC controls, and plasma samples and then incubated overnight at 4°C in the dark while shaking at 800 rpm. The next day, after 3 washes in proprietary wash buffer, detection bodies were added and incubated in the dark at room temperature (RT) for 30 minutes of shaking, followed by the addition of Streptavidin-Phycoerythrin for 30 minutes shaking at RT. The samples were washed 3 times and resuspended in wash buffer for subsequent acquisition on a Luminex MAGPIX with xPONENT v. 4.1 software. Complimentary analysis by Millipore using their Belysa curve-analysis software determined analyte quantification of the samples from the Median Fluorescent Intensity (MFI) data using a 5-parameter logistic or spline curve-fitting method. Additional cytokines were analyzed similarly (IL1a, IL1b, M-CSF, G-CSF, GM-CSF, IFN-γ, IL-10, and IL-4, all custom picked from Millipore's MCYTOMAG-70K kit).

Singleplex assay for adiponectin

Similarly to the Milliplex assay, plasma samples were analyzed for adiponectin using the Millipore Mouse Adiponectin Single Plex Magnetic Bead Kit.

FACS

Stromal vascular fraction (SVF) cells were isolated from mouse epididymal and subcutaneous white adipose tissue (eWAT and sWAT) and digested in buffer containing 0.8 mg/ml of collagenase II for 30 and 45 minutes, respectively, at 37°C in a shaker set to 200 rpm. After 10 minutes of 300 x g centrifugation at 4°C, the pellets were washed with RPMI (supplemented with 10% fetal bovine serum (FBS) and 1% penicillin-streptomycin) through a 70 μm strainer. Red blood cells were lysed for 2 minutes at RT and the SVF cells were washed through a 40 μm strainer. Cells were resuspended in HBSS for subsequent flow cytometry staining.

SVF cells were stained in 100 μl Zombie Aqua (1:4000 dilution in HBSS) fixable viability dye for 30 min at 4°C in the dark. Cells were then centrifuged at 300 x g for 10 min and resuspended in Fc Block (mAb CD16/CD32, 1:400 dilution in stain/wash/sort buffer (PBS with 0.5% bovine serum albumin (BSA) and 1mM EDTA)) and incubated at 4°C for 15 minutes, then stained in a cocktail of antibodies shown in the key resources table along with BD Horizon Brilliant Stain Buffer and True-Stain Monocyte Blocker added to the sample for a final volume of 100 μl, for 45 min at 4°C in the dark. After washing twice (centrifugation at 300 x g for 10 minutes), the cells were fixed with 2% formaldehyde in PBS for 15 minutes at 4°C, washed twice (centrifugation at 800 x g for 5 minutes), and resuspended in wash buffer for overnight storage at 4°C. Unstained, single-stained (on compensation beads and/or cells), and a complete set of FMO controls

underwent a similar preparation process alongside the staining of the test samples. Flow cytometry acquisition was performed the following morning on a Cytek Biosciences Aurora with SpectroFlo software. Batch-to-batch and instrumental settings consistency was controlled by running a sample of Ultra Rainbow Fluorescent Particles before each experiment, in addition to daily QC. An autofluorescence tag with peak emission in the 405 525/17 nm (Channel V7) from the unstained control was incorporated into the panel of reference controls. The unmixed data were then analyzed with FlowJo software. Macrophages were gated as follows: Cells (FSC-H, SSC-H) > Single Cells (SSC-A, SSC-H) > Live (Viability, SSC-H) > $CD45^+$ (CD45, FSC-H) > Macs (CD11b, F4/80) > $CD64^+$ Macs (CD11b, CD64).

Isolation of $CD64^+$ cells

SVF cells were isolated as above. After incubating with Fc block for 15 minutes at 4°C, 25 µl of streptavidin magnetic beads (ThermoFisher 11205D) preloaded with 3 µg of biotin-CD64 (Biolegend 139318) was added to the cells. The mixture was rotated at 4°C for 20 minutes. The $CD64^+$ cells were isolated and washed, then immediately processed for total RNA extraction with Qiagen RNeasy Micro kit (74004).

RNAseq

Total RNA from eWAT was extracted using a combination of TRIzol™ reagent (ThermoFisher 15596026) and the PureLink™ RNA mini kit (Invitrogen 12183018A). Approximately 80 mg of eWAT was lysed with the TRIzol™ and the aqueous layer was ethanol precipitated and cleaned up with the PureLink™ RNA mini kit. The total RNA was submitted to the Van Andel Institute genomics core for libraries preparation and sequencing. Libraries were prepared from 500 ng of total RNA using the KAPA Stranded mRNA-Seq Kit (v4.17) (Kapa Biosystems, Wilmington, MA USA). RNA was sheared to 300–400 bp. Prior to PCR amplification, cDNA fragments were ligated to IDT for Illumina TruSeq UD Indexed adapters (Illumina Inc, San Diego CA, USA). Quality and quantity of the finished libraries were assessed using a combination of Agilent DNA High Sensitivity chip (Agilent Technologies, Inc.), QuantiFluor® dsDNA System (Promega Corp., Madison, WI, USA), and Kapa Illumina Library Quantification qPCR assays (Kapa Biosystems). Individually indexed libraries were pooled and 50 bp, paired end sequencing was performed on an Illumina NovaSeq6000 sequencer using an S1, 100 bp sequencing kit (Illumina Inc., San Diego, CA, USA) to an average depth of 40M reads per sample. Base calling was done by Illumina RTA3 and output of NCS was demultiplexed and converted to FastQ format with Illumina Bcl2fastq v1.9.0

For RNAseq of $CD64^+$ cells, RNA was extracted with Qiagen RNeasy Micro kit (74004). Libraries were prepared by the Van Andel Institute genomics core from 1–5 ng of total RNA. Total RNA material was converted to dsDNA using the SMART-Seq v4 Ultra Low Input RNA Kit for Sequencing, v. 091817 (Takara Bio USA, Mountain View, CA, USA). cDNA was sheared to 200–500 bp using a Covaris E220 Evolution ultrasonicator (Covaris Inc., Woburn, MA USA) and Illumina compatible sequencing libraries were generated using the Kapa HyperPrep kit, v6.17 (Kapa Biosystems, Wilmington, MA USA). Prior to PCR amplification, cDNA fragments were ligated to Bioo Scientific NEXTflex dual adapters (Bioo Scientific, Austin, TX, USA). Quality and quantity of the finished libraries were assessed using a combination of Agilent DNA High Sensitivity chip (Agilent Technologies, Inc.), QuantiFluor® dsDNA System (Promega Corp., Madison, WI, USA), and Kapa Illumina Library Quantification qPCR assays (Kapa Biosystems). Individually indexed libraries were pooled and 50 bp, paired-end sequencing was performed on an Illumina NovaSeq6000 sequencer using an SP, 100 cycle sequencing kit (Illumina Inc., San Diego, CA, USA) and each library was sequenced to an average raw depth of 30M reads. Base calling was done by Illumina RTA3 and output of NCS was demultiplexed and converted to FastQ format with Illumina Bcl2fastq v1.9.0.

qPCR

For qPCR, total RNA was reverse-transcribed into cDNA using SuperScript IV Vilo Mastermix (Invitrogen). Primer sets used were *acaca*-forward 5′- ATGGGCGGAATGGTCTCTTTC, *acaca*-reverse 5′- TGGGGACC TTGTCTTCATCAT; *ffar2*-forward 5′- ATCCTCCTGCTTAATCTGACCC, *ffar2*-reverse 5′- CGCACACGAT CTTTGGTAGGT. For statistics, an unpaired Student's *t* test was performed using GraphPad Prism version 8.00 for Windows, GraphPad Software, La Jolla, California, USA.

Bioinformatics (mRNA-seq data processing and analysis)

Reads were aligned to the mm10 genome (GENCODE M24) using STAR v2.7.8a.[58] Gene counts from STAR were imported into R v4.1.0 for downstream analysis. Pairwise contrasts of knockout versus wildtype were

tested by modeling the samples from the B6 macrophages, eWAT under ketogenic diet, or eWAT under normal diet separately using the quasi-likelihood F-test workflow in edgeR v3.34.1.[59,60] Additive models consisting of the genotype and litter variables (~0+Genotype+Litter) were fitted. Significant genes were identified using an adjusted p-value cutoff of 0.05. Volcano plots were created using EnhancedVolcano v1.10.0.

For identifying genes that had a different genotype effect between the ketogenic and normal diets, the eWAT samples from the two diets were modeled together using DESeq2 v1.32.0.[61] Because specific litters were present in each diet, we followed the DESeq2 vignette for fitting a nested model. Briefly, the design matrix was created based on the formula, '~ Diet + Diet:Litter.n + Diet:Genotype', but columns containing only zeroes were removed. The interaction between genotype and diet was tested using the contrast of the "DietKeto.GenotypeAKO" and "DietCon.GenotypeAKO" coefficients with an adjusted p-value cutoff of 0.05. Gene expression heatmaps were created using pheatmap v1.0.12 or ComplexHeatmap v2.8.0[62] based on variance-stabilized transformed counts computed using DESeq2. Ribosome-related genes were identified based on gene symbols beginning with 'Mrpl' or 'Mrps'. Electron transport chain genes were identified from MitoCarta3.0[65] by searching for the pattern, "Complex\\s+[66]". Transcription factor genes were identified using biomaRt v2.48.3[63] to filter for genes annotated with the 'GO:0003700' GO term.

Genes that had significant interaction effects were clustered using the Z-scores of the variance-stabilized transformed counts and a k-means approach, using the kmeans function in the base R stats package with the parameters, 'centers = 5, nstart = 25'. The value for 'k' was selected using an elbow plot as implemented in the fviz_nbclust function in factoextra v1.0.7. Pathway enrichment for each cluster was tested using hypergeometric tests as implemented in clusterProfiler v4.0.5[64] with the union of the genes across all clusters as the background. Entrez gene IDs and GO term annotations were obtained from the org.Mm.eg.db v3.13.0 package.

QUANTIFICATION AND STATISTICAL ANALYSIS

Unless otherwise stated, graphs were created and statistical significance determined with GraphPad Prism using unpaired two-tailed Student's *t* test for calculating p-values for pairwise comparisons and ordinary one-way ANOVA multiple comparisons test for more than 2 groups. *** means $p < 0.001$, ** means $0.001 < p < 0.01$, and * means $0.01 < p < 0.05$.